Experimental estimation of the Lorenz number and scattering parameter for *p*-type bismuth antimony telluride via multiple doping under constant temperature conditions

Jun Asai[a], Mongkol Bumbrungpon[b], Toshiya Tsubochi[a], Takayuki Kanaya[a], Masaya Tachii[a], Toshiki Maeda[a], Taku Iwamoto[c], Chika Kanda[c], Kazuhiro Hasezaki[d]

[a]*Department of Mechanical Science, Division of Science and Technology, Graduate School of Sciences and Technology for Innovation, Tokushima University, 2-1 Minamijyousanjima, Tokushima 770-8506, Japan*

[b]*Graduate School of Advanced Technology and Sciences, Tokushima University, 2-1 Minamijyousanjima, Tokushima 770-8506, Japan*

[c]*Department of Science and Technology, Faculty of Science and Technology, Tokushima University, 2-1 Minamijyousanjima, Tokushima 770-8506, Japan*

[d]*Department of Mechanical Science, Graduate School of Technology, Industrial and Social Sciences, Tokushima University, 2-1 Minamijyousanjima, Tokushima 770-8506, Japan*

**Corresponding author: hasezaki@tokushima-u.ac.jp*

The effects of the addition of lead as one of the multiple dopants in *p*-type $Bi_{0.3-x}Sb_{1.7}Te_{3.0+0.01}Pb_x$ (x = 0, 0.001, 0.002, 0.003) fabricated by mechanical alloying followed by hot pressing were investigated. Measurements by X-ray diffraction (XRD), differential thermal analysis (DTA), and scanning electron microscopy (SEM) showed the same matrix morphology. The second phase by doped elements was not confirmed by transmission electron microscopy (TEM). By using the lead addition results and previously studied tellurium doping effects, the Lorenz number L was evaluated to be 0.73–1.18 × 10^{-8} W S^{-1} K^{-2}. The scattering parameter γ and reduced Fermi energy η were estimated by using expressions on the basis of a one-electron approximation, measured Seebeck coefficients, and the estimated L at room temperature. The γ ranged approximately from −1.06 to −0.60 and showed a mutual effect of acoustic and optical phonon scattering. The relationship between a dimensionless figure of merit ZT and η was clarified. The optimum η was determined as −1.25 at ZT = 1.26. From these results, multi-doped $Bi_{0.3}Sb_{1.7}Te_{3.0}$ could be applied to evaluate L, γ, and η at a constant temperature.

Keywords: Electrical properties; Thermal conductivity; Hot pressing; Thermoelectric materials

1. Introduction

Thermoelectric materials can convert thermal energy into electricity directly and vice versa by the Seebeck effect and Peltier effect respectively, with potential applications such as power generation and solid-state cooling. Thermoelectric devices consisting of such materials have many advantages, such as a lack of mechanically moving parts, high reliability, lightness, and environmental friendliness [1,2]. However, thermoelectric technology is currently limited to niche applications due to moderate efficiency and a relatively high cost [3]. The development of methods for improving thermoelectric performance and understanding of its improved mechanism are therefore still the central aim of much research. Various thermoelectric materials, such as Bi_2Te_3 [4–6], PbTe [7,8], metal oxides [9,10], half-Heusler [11,12], Zintl phases [13,14], etc. have been studied to improve their thermoelectric performance in recent years.

The thermoelectric performance of the materials is evaluated by a dimensionless figure of merit *ZT*:

$$ZT = \frac{\alpha^2 \sigma}{\kappa} T \quad (1)$$

where α is the Seebeck coefficient (V K^{-1}), σ is the electrical conductivity (S m^{-1}), κ is the thermal conductivity (W m^{-1} K^{-1}), and T is the absolute temperature (K) [15]. The thermal conductivity κ generally includes phonon and carrier contributions:

$$\kappa = \kappa_{\text{phonon}} + \kappa_{\text{carrier}} = \kappa_{\text{phonon}} + L\sigma T. \quad (2)$$

The carrier contribution, κ_{carrier}, is given by the Wiedemann-Franz law, where κ_{phonon} is the phonon contribution and L is the Lorenz number [16]. The Lorenz number L is given by the following expression on the basis of a one-electron approximation or single parabolic band model [17,18]:

$$L = \left(\frac{k_B}{e}\right)^2 \left\{\frac{(1+\gamma)(3+\gamma)F_\gamma(\eta)F_{\gamma+2}(\eta) - (2+\gamma)^2 F_{\gamma+1}(\eta)^2}{(1+\gamma)^2 F_\gamma(\eta)^2}\right\} \quad (3)$$

where η is the reduced Fermi energy (= E_F/k_BT, E_F: Fermi energy, k_B: Boltzmann's constant), γ is the scattering parameter, and $F_\gamma(\eta)$ is the Fermi integral. The transport properties of a conductor including thermoelectric materials depend not only on the concentration of the charge carrier but also on the mean free path length between collisions. The scattering parameter is representative of collision effects. The scattering parameter is an important parameter for understanding thermoelectric properties. The reduced Fermi energy η is usually found from the experimental values of the Seebeck coefficient as follows [17,18]:

$$\alpha = \pm\frac{k_B}{e}\left(\frac{(2+\gamma)F_{\gamma+1}(\eta)}{(1+\gamma)F_\gamma(\eta)} - \eta\right). \quad (4)$$

The Fermi integral is defined by

$$F_\gamma(\eta) = \int_0^\infty \frac{\epsilon^\gamma d\epsilon}{1+\exp(\epsilon-\eta)} \quad (5)$$

where ε is the electronic energy (eV). The scattering parameter γ is identified for several

scattering mechanisms, i.e., the parameter $\gamma = 0.5$ for neutral impurity scattering, $\gamma = 0$ for acoustic phonon scattering, and $\gamma = -1.0$ for both acoustic and optical phonon scattering [19–22]. These thermoelectric properties of Eqs. (1)–(5) strongly depend on the temperature.

For room-temperature applications, Bi_2Te_3-based materials have received increasing attention due to their high thermoelectric performance near room temperature [23]. They have a rhombohedral crystal structure with the $R\bar{3}m$ space group. Their thermoelectric properties, especially their electrical and thermal conductivities, and physical properties are significantly anisotropic [24]. Mechanical alloying (MA) followed by hot pressing (HP) is one of the preparation methods for polycrystalline Bi_2Te_3 materials that is widely studied [25–27]. MA is a high-energy powder processing method that has a grain-refining effect via grain boundary scattering. The sintered compacts obtained via the MA-HP process have random crystal orientations and refined structures, which decrease the phonon thermal conductivity [25].

Recently, a huge variety of strategies have been used to improve the thermoelectric performance of Bi_2Te_3 materials, such as doping with various elements [28–34], dispersing nanomaterials that dramatically reduce the thermal conductivity [35–38], and introducing processing techniques such as annealing, two-step sintering, and hydrogen

reduction treatment [39–42]. In a previous study, the optimal Bi-Sb ratio for undoped Bi_2Te_3-Sb_2Te_3 solid solution produced by the MA-HP process was determined to be $Bi_{0.3}Sb_{1.7}Te_{3.0}$ [43], which differs from the best composition of the sample produced by established melt growth methods, such as zone melting of the Bridgman method, namely, $Bi_{0.5}Sb_{1.5}Te_{3.0}$ [44]. In addition, the importance of the milling vessel material became apparent by comparing the thermoelectric properties of $Bi_{0.3}Sb_{1.7}Te_{3.0}$ fabricated with YSZ ceramic (yttria-stabilized zirconia) milling vessels and stainless-steel metal vessels. Ceramic milling vessels suppressed contamination from milling vessels and improved the thermoelectric performance by 15% compared with conventional stainless-steel vessels [45]. Furthermore, by adding small excess tellurium, the thermoelectric performance of bismuth antimony telluride was improved and reached the maximum ZT = 1.30 at room temperature when the composition was $Bi_{0.3}Sb_{1.7}Te_{3.01}$. Tellurium doping did not affect the matrix morphology and gave constant phonon thermal conductivity and an improved power factor due to the small content of the dopant [28]. On the other hand, as the tellurium solid solubility limit was quite narrow, the variation ranges of the electrical conductivity and Seebeck coefficient were small. Controlling the electrical properties in a wider range is crucial not only to improve thermoelectric performance at room temperature but also to produce thermoelectric

materials working at mid-temperature [46,47]. Since lead is a group 14 element close to bismuth, which is a group 15 element, lead is a typical element that is added as a single dopant into *p*-type bismuth telluride [30,31]. Therefore, we added additional lead, which works as an effective acceptor, into $Bi_{0.3}Sb_{1.7}Te_{3.0+0.01}$ to vary the electrical properties in a wider range.

Although multiple doping was implemented for *n*-type bismuth telluride to improve *ZT* and to optimize the carrier concentration, the effect of multiple doping and variation range of the electrical properties were almost the same as single doping [48]. However, the multiple doping effect for *p*-type $Bi_{0.3}Sb_{1.7}Te_{3.0}$ fabricated by the MA-HP process with ceramic milling vessels has not been investigated previously. The present study was undertaken to investigate the effect of adding lead as one of the multiple dopants in $Bi_{0.3}Sb_{1.7}Te_{3.0+0.01}$. In addition, the Lorenz number *L* was estimated from Eq. (2) by using the doping results. The Lorenz number *L* is an important factor to evaluate the phonon thermal conductivity and was generally assumed to be $1.6–2.45 \times 10^{-8}$ W S^{-1} K^{-2} [31,43,49,50]. In the present study, the Lorenz number *L* was empirically estimated by using the relationship of thermal and electrical conductivities under constant κ_{phonon} from Eq. (2), which differed from the reported method with measuring the temperature dependence of thermoelectric parameters [51,52]. Finally, the scattering parameter γ and

reduced Fermi energy η were estimated from Eqs. (3)–(5) by using the measured Seebeck coefficients and estimated Lorenz number under constant temperature. A series of investigations for Bi_2Te_3 were conducted by evaluating the carrier concentration [5,31,34], while there are few reports that evaluate Bi_2Te_3-based materials from the perspective of the scattering parameter γ [22]. Furthermore, the scattering parameter γ of the sample fabricated by the MA-HP process with ceramic vessels has not been investigated. This is because each thermoelectric parameter highly depends on temperature, and these values lack reliability. Thus, the Lorenz number, scattering parameter, and reduced Fermi energy near the maximum ZT of $Bi_{0.3}Sb_{1.7}Te_{3.0}$ fabricated by the MA-HP process were clarified by evaluating those under constant temperature conditions.

2. Experimental

High-purity bismuth (99.999%), antimony (99.9999%), tellurium (99.9999%), and lead (99.99%) purchased from Kojundo Chemical Laboratory Co., Ltd., Saitama, Japan were weighed to give various stoichiometries of $Bi_{0.3-x}Sb_{1.7}Te_{3.01}Pb_x$ (x = 0–0.003) and $Bi_{0.3}Sb_{1.7}Te_{3.0+y}$ (y = 0–0.0085). The elements were loaded into YSZ milling vessels with YSZ balls with a diameter of 25 mm. The weight ratio of the balls to the raw elements was 20:1. The vessels were sealed in a glove box under an argon environment. The raw elements were powdered and alloyed by dry milling with a Fritsch P-5 planetary ball mill at a rotational speed of 150 rpm for 30 h. The milled powder was sieved with a 150 μm diameter sieve. It was confirmed that no raw material remained. The powder was sintered by hot pressing at 350°C under a uniaxial pressure of 147 MPa. The sintered bulk consisted of a cylinder with a height of 9 mm and a diameter of 10 mm. The bulk was cut into disks with a thickness of 1.0 mm and a diameter of 10 mm. The disks cut from both ends of the cylinder were discarded because it has been reported that these portions contain (00l) texture formation [53,54].

The phase structures in the out-of-plane direction of sintered disks with x = 0 and 0.003 were examined by X-ray diffraction (XRD; Rigaku SmartLab) with Cu Kα radiation. All disks were examined in the Bragg angle range 2θ = 10°–110°, with a step size of

0.1° and step speed of 5.0 s per step. The orientation factor F of each disk was calculated by using the Lotgering method to confirm isotropy. F is expressed by the following equations [55]:

$$F = \frac{P - P_0}{1 - P_0} \quad (6)$$

$$P = \frac{\sum I(00l)}{\sum I(hkl)} \quad (7)$$

$$P_0 = \frac{\sum I_0(00l)}{\sum I_0(hkl)} \quad (8)$$

where $\Sigma I(00l)$ and $\Sigma I(hkl)$ are the sum of the $(00l)$ and (hkl) reflection intensities, respectively. P is the ratio of $\Sigma I(00l)$ and $\Sigma I(hkl)$, which shows the observed degree of orientation for the obtained disk. P_0 is the same ratio for powder with random orientation. Composites with $F = 0$ have no oriented texture, while grains are fully oriented when $F = 1$ [43]. $P_0 = 0.0486$ was estimated from standard peaks of $Bi_{0.3}Sb_{1.7}Te_{3.0}$ (Inorganic Crystal Structure Database (ICSD) #184248) [56]. The densities of the sintered disks with $x = 0$, 0.003 and $y = 0$, 0.006 were measured by using Archimedes' method at room temperature. The accuracy of the densities was within ±1%.

Differential thermal analysis (DTA; Hitachi TG/DTA6300) was conducted for the ground disks with $x = 0$ and 0.003 to confirm the existence of elemental Te or alloyed PbTe. DTA was performed in the temperature range of 30–950°C at a constant heating

rate of 10°C min^{-1} under Ar gas flow.

The cross-sectional microstructures and the in-plane fracture surfaces of the sintered disk with x = 0 and 0.003 were investigated using scanning electron microscopy (SEM; JEOL, JSM-6510A) to confirm that no variation in morphology occurred due to the addition of tellurium and lead dopants. To confirm whether the second phase was formed by elemental doping, the elemental dispersions in cross-sections of the sintered disk with x = 0.003 were investigated by transmission electron microscopy (TEM; JEOL, JEM-2100F).

The thermoelectric properties (the Seebeck coefficient, electrical conductivity, and thermal conductivity) at room temperature of all the sintered disks were determined using laboratory-constructed systems. The dimensionless figure of merit, ZT, at room temperature (27°C) was estimated using Eq. (1). The Seebeck coefficients were measured by the thermal contact method [57]. The standard material SRM3451 was used to confirm that the measurement accuracy was within ±2% [58]. The electrical conductivities were measured by the four-point probe method using a delta mode electrical resistance system based on a 2182A/6220 instrument (Keithley Instruments, Inc.). The probe was made of tungsten carbide and 1.00 mm in diameter. All measurements made using the system were confirmed by ohmic contact. The accuracy

of the measured electrical conductivity was within ±1% [59]. The thermal conductivities were measured under a 1 Pa vacuum by using a static comparison method [48,60]. A quartz disk with a diameter of 10 mm and a thickness of 1.0 mm was used as standard material (κ = 1.411 W m^{-1} K^{-1}). The accuracy of the thermal conductivity was within ±1%.

3. Results and Discussion

All sintered samples were *p*-type semiconductors according to the measured Seebeck coefficient. Figure 1 shows XRD patterns of the sintered samples with $x = 0$ and 0.003. Each peak of both samples corresponded with the standard peaks of $Bi_{0.3}Sb_{1.7}Te_{3.0}$ (Inorganic Crystal Structure Database (ICSD) #184248), and no other decomposed or precipitated phases, such as pure lead or lead telluride, were detected [56]. The estimated F values by using Eqs. (6)–(8) for $x = 0$ and 0.003 were 0.046 and 0.036, respectively, which indicated that preferred orientation in the (00*l*) direction was not observed for the resulting samples [61]. These results indicated that the additive lead and tellurium had no effects on the XRD pattern of $Bi_{0.3}Sb_{1.7}Te_{3.0}$ and the orientation of the (00*l*) planes. Table 1 shows the measured absolute density and relative density. The theoretical density value of 6.73×10^3 kg m^{-3} for $Bi_{0.3}Sb_{1.7}Te_{3.0}$ was used for all of the measured samples due to a sufficiently small amount of dopants [56]. The relative densities of all measured samples exceeded 99%, and no difference was confirmed.

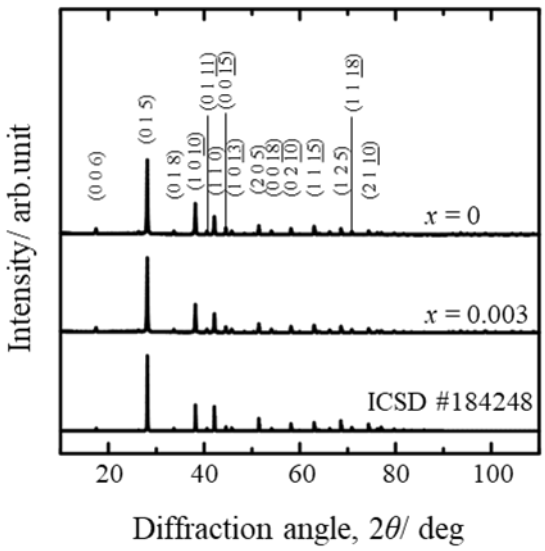

Fig. 1 XRD patterns (2θ = 10–110°) of $Bi_{0.3-x}Sb_{1.7}Te_{3.01}Pb_x$ (x = 0, 0.003) sintered disks prepared by MA-HP and $Bi_{0.3}Sb_{1.7}Te_{3.0}$ main indices [56]. The standard peaks correspond to $Bi_{0.3}Sb_{1.7}Te_{3.0}$ (ICSD #184248).

Table 1 Absolute and relative densities of $Bi_{0.3-x}Sb_{1.7}Te_{3.01}Pb_x$ and $Bi_{0.3}Sb_{1.7}Te_{3.0+y}$.

Composition $Bi_{0.3-x}Sb_{1.7}Te_{3.01}Pb_x$ $Bi_{0.3}Sb_{1.7}Te_{3.0+y}$	Absolute density [$\times 10^3$ kg m^{-3}]	Relative density [%]
x = 0	6.67 ± 0.07	99.1 ± 1
x = 0.003	6.70 ± 0.07	99.5 ± 1
y = 0	6.69 ± 0.07	99.4 ± 1
y = 0.006	6.67 ± 0.07	99.1 ± 1

Theoretical density 6.73 × 10^3 kg m^{-3} for $Bi_{0.3}Sb_{1.7}Te_{3.0}$ [56]

Figure 2 shows the DTA results for the samples with x = 0 and 0.003. The endothermic point at approximately 600°C corresponds to the melting point of $Bi_{0.3}Sb_{1.7}Te_{3.0}$. The endothermic peak due to the melting of pure lead (327°C) or lead telluride (924°C) was not detected. The additive lead did not affect the DTA result. This may be because the additive lead content of the sample was sufficiently small and dissolved in the matrix.

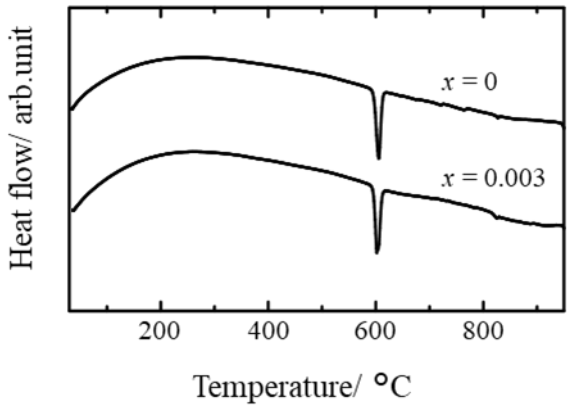

Fig. 2 DTA curves for pestle-ground, sintered disks of $Bi_{0.3-x}Sb_{1.7}Te_{3.01}Pb_x$ (x = 0 and 0.003) prepared by MA-HP.

Figure 3 (a) and (b) show the cross-sectional SEM micrographs for x = 0 and 0.003, respectively. Both of the samples were dense and homogeneous throughout the sample. An obvious difference in the matrix morphology was not observed. Figure 3 (c) and (d) show SEM micrographs of the fracture surfaces of the samples with x = 0 and 0.003,

respectively. An obvious difference in the grain size was not observed. The grain size of both samples was almost the same and approximately 1 μm. The results show that the additive lead had no effect on grain growth.

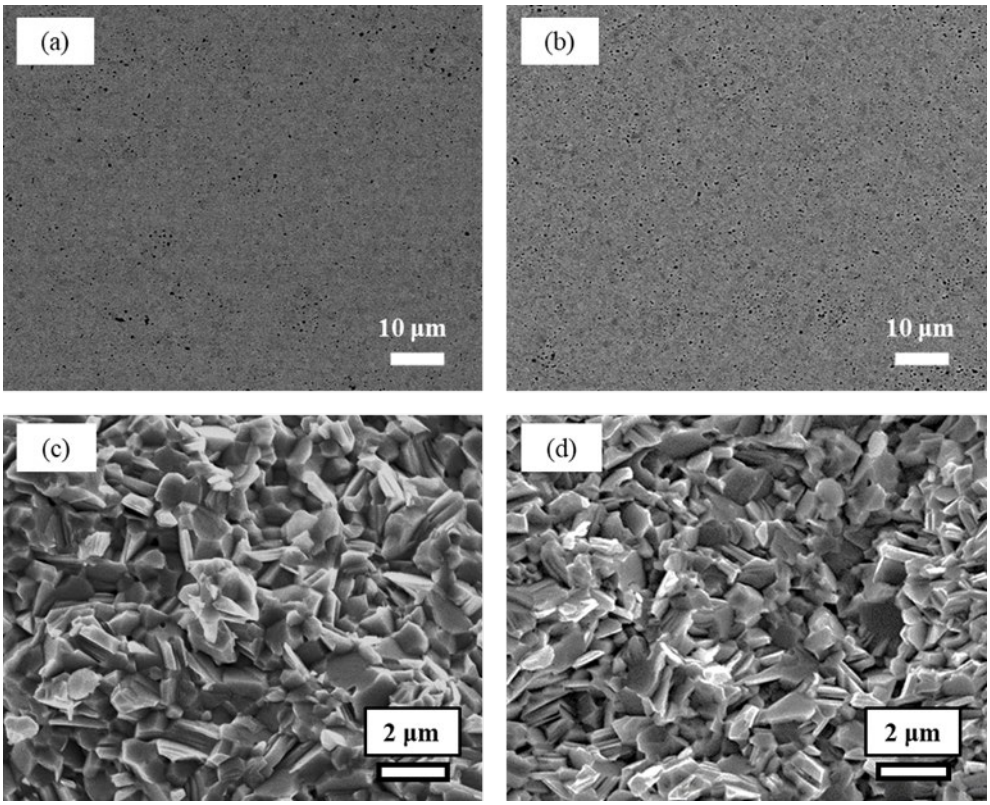

Fig. 3 SEM micrographs of the cross-section of sintered disks with (a) $x = 0$ and (b) $x = 0.003$. SEM micrographs of the fracture surface of sintered disks with (c) $x = 0$ and (d) $x = 0.003$.

Figure 4 (a) shows the STEM micrograph of the sample with $x = 0.003$. The grain size is approximately 1 μm, which corresponds to the fracture surface observation by SEM.

Figure 4 (b)−(e) show the elemental distributions of Sb, Te, Bi, and Pb. Each element was distributed homogeneously, and the second phase was not observed. From these results, the obtained $Bi_{0.3-x}Sb_{1.7}Te_{3.01}Pb_x$ with x = 0–0.003 has the same morphology due to the small contents of dopants. In addition, it was also reported in the literature that the phonon thermal conductivity is not changed at a small level addition of lead [30,31]. Therefore, it was expected that the phonon thermal conductivity was almost constant.

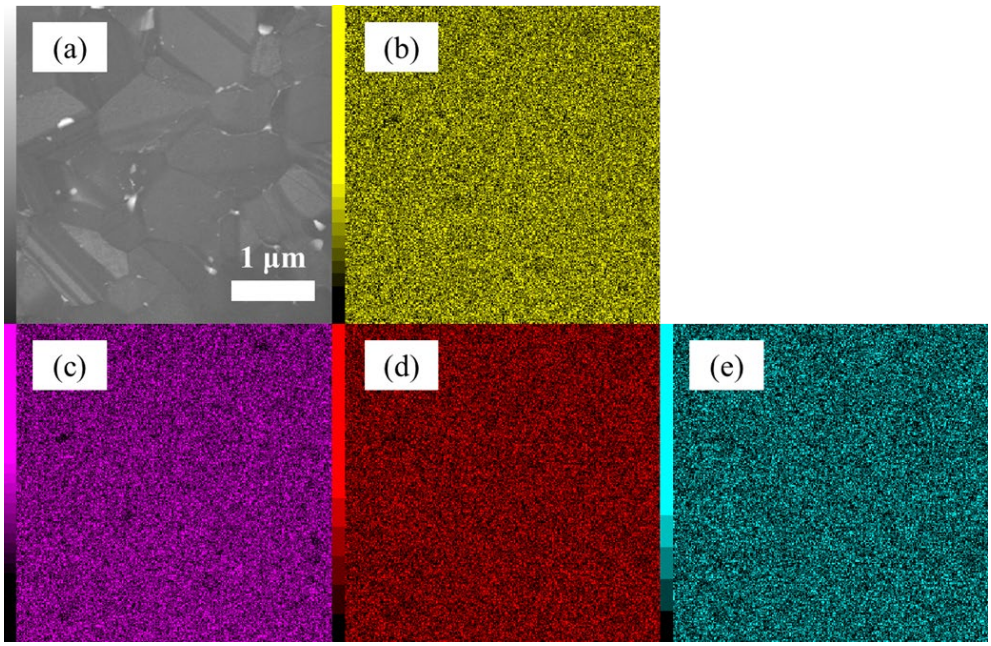

Fig. 4 (a) A STEM micrograph of the cross-section of the sintered disk with x = 0.003 and the elemental distributions of (b) Sb, (c) Te, (d) Bi, and (e) Pb determined by EDS.

Figure 5 (a) shows the relationship between the Seebeck coefficient at room temperature

and the additive lead content *x*. All of the measured Seebeck coefficients were positive, which indicated that they were *p*-type semiconductors. The Seebeck coefficient decreased monotonically with increasing additive lead content. Figure 5 (b) shows the relationship between the electrical conductivity at room temperature and the additive lead content. The electrical conductivity increased monotonically with increasing additive lead content. The trend of the variation in the electrical conductivity was opposite to that of the Seebeck coefficient, which indicated that the additive lead acted as a hole carrier dopant. The results showed that the variation range in electrical properties became wider by adding lead as an additional dopant, compared with only tellurium doping [28,62]; however, the lead added as one of multiple dopants performed the same function as when added as a single dopant [31], and the specific effect of multiple doping was not confirmed.

Figure 5 (c) shows the relationship between the thermal conductivity at room temperature and the additive lead content. The phonon and carrier thermal conductivities were estimated by using Eq. (2). The Lorenz number *L* was temporarily assumed to be the standard Lorenz number L_0 for metals as

$$L_0 = \frac{\kappa_{\text{carrier}}}{\sigma T} = \frac{\pi^2}{3}\frac{k_B^2}{e^2}. \quad (9)$$

The numerical value of L_0 is approximately 2.45×10^{-8} W S^{-1} K^{-2} [60]. The total

thermal conductivity increased with increasing lead addition. The greater part of the difference in the total thermal conductivities is due to carrier-induced thermal conductivity. The phonon thermal conductivity decreased with increasing lead addition. The result does not correspond to the fact that the additional lead dissolved in the matrix did not affect grain growth, as shown in DTA and SEM observations. It was considered that the used Lorenz number ($L_0 = 2.45 \times 10^{-8}$ W S^{-1} K^2) was overestimated, which led to the mismatch between the prediction and the results in phonon thermal conductivities. Figure 5 (d) shows the relationship between the dimensionless figure of merit *ZT* at room temperature and the additive lead content. At $x = 0$, the maximum *ZT* value of 1.26 was obtained and *ZT* decreased with increasing additive lead content. At $0.001 \leq x \leq 0.003$, *ZT* varied from 1.18 to 1.09. The deteriorated *ZT* was attributed to the overbalance of carrier concentration for the thermoelectric material intended for room temperature.

These results show that multiple doping of lead in $Bi_{0.3}Sb_{1.7}Te_{3.01}$ is an effective way to control the carrier concentration without variation of the condition of the BiSbTe matrix, such as the crystal structure and grain size.

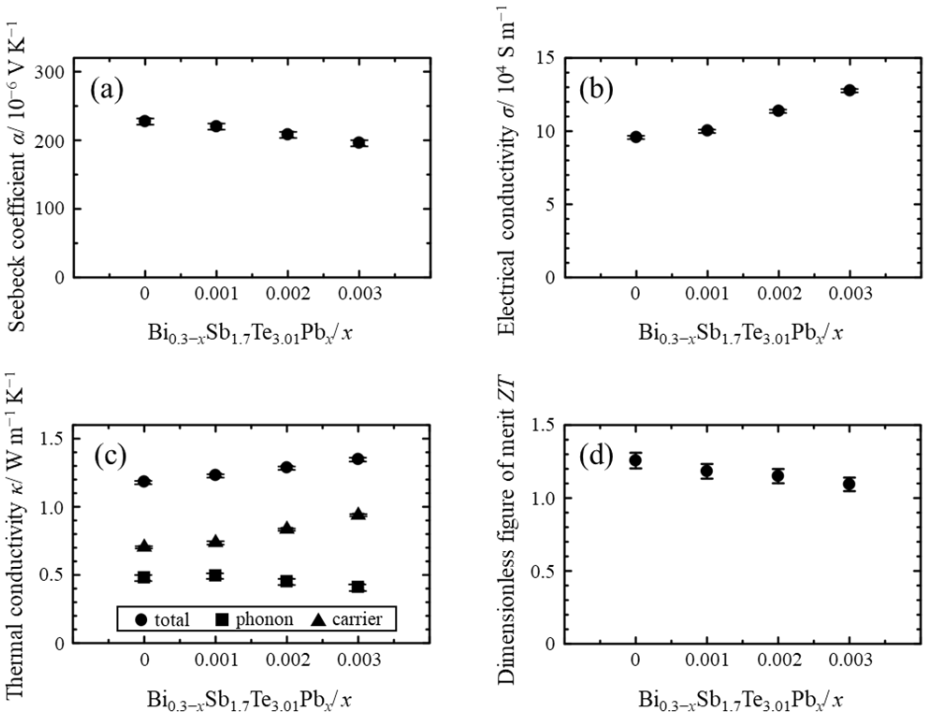

Fig. 5 The relationships between the room-temperature thermoelectric properties and the amount of additive lead (x) for $Bi_{0.3-x}Sb_{1.7}Te_{3.01}Pb_x$. (a) Seebeck coefficient, (b) electrical conductivity, (c) thermal conductivity, and (d) dimensionless figure of merit (ZT).

In the present study, the same matrix conditions were observed due to the small amount of dopants. In addition, it was reported by other groups that the additive lead less than 0.1 at% or additive tellurium less than 8 at% had no effect on phonon thermal conductivity and resulted in almost the same value of κ_{phonon} [30,31,39]. Therefore, we assumed that the phonon thermal conductivity in this study could be regarded as a constant value. Furthermore, it was also confirmed in a previous study that additive

tellurium less than 0.2 at% does not affect matrix grain growth or phonon thermal conductivity [28]. From these results, we considered that the Lorenz number L could be evaluated by using Eq. (2) and the doping results of lead and tellurium, assuming that the κ_{phonon} was constant.

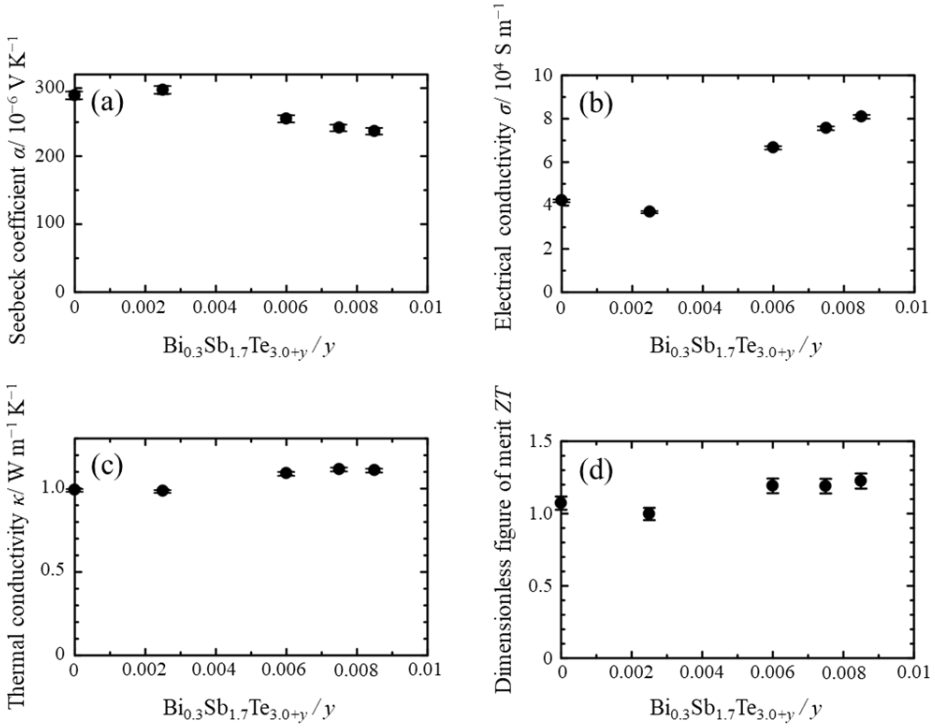

Fig. 6 The relationships between the room-temperature thermoelectric properties and the amount of additive tellurium (y) for $Bi_{0.3}Sb_{1.7}Te_{3.0+y}$. (a) Seebeck coefficient, (b) electrical conductivity, (c) thermal conductivity, and (d) dimensionless figure of merit (ZT).

Figure 6 shows the relationship between the room-temperature thermoelectric properties and the amount of additive tellurium (y) for $Bi_{0.3}Sb_{1.7}Te_{3.0+y}$. Additive tellurium acted as a hole carrier dopant in the range of $y \geq 0.0025$. On the other hand, additive tellurium supplemented the tellurium deficiency at $y \leq 0.0025$. These results correspond to previously reported results, and the same matrix conditions at $y \leq 0.01$ were confirmed in a previous study [28,62].

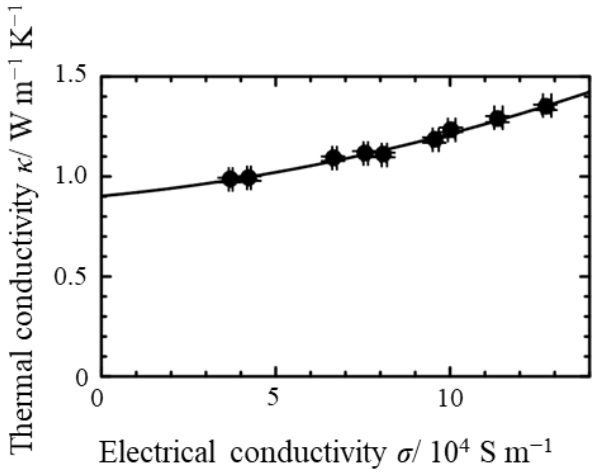

Fig. 7 The relationship between thermal and electrical conductivity. The quadratic curve shows $\kappa = (1.50 \times 10^{-11}\sigma + 1.62 \times 10^{-6})\sigma + 0.902$.

Figure 7 shows the relationship between the total thermal conductivity κ and the electrical conductivity σ for all the samples doped with tellurium and lead. When the phonon thermal conductivity κ_{phonon} is assumed to be constant and the absolute

temperature T is fixed at room temperature, κ is expressed as a function of σ and Lorenz number L. L is strictly expressed by Eq. (3), but it is complicated to use it. Besides, in theory the $\kappa_{carrier}$ increases non-linearly with increasing electrical conductivity [44]. Therefore, κ was approximated as a quadratic function of σ for the sake of simplicity. As a result of fitting by the least-squares method, κ is expressed as $\kappa = (1.50 \times 10^{-11}\sigma + 1.62 \times 10^{-6})\sigma + 0.902$ at room temperature. The linear regression yielded a determination coefficient R^2 of 0.99, indicating a reasonable evaluation. From Eq. (2), the constant phonon thermal conductivity at room temperature was estimated to be 0.902 W m^{-1} K^{-1}.

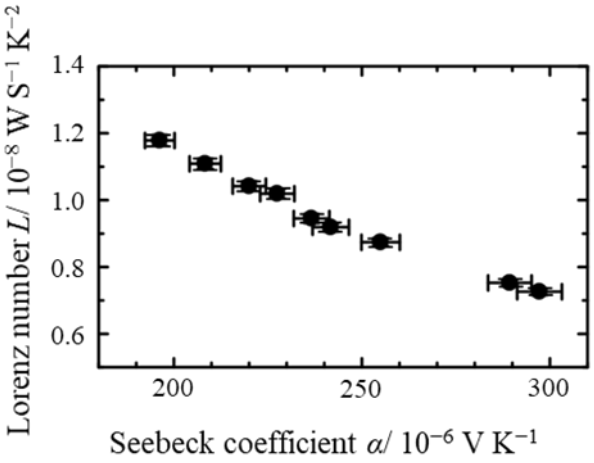

Fig. 8 The relationship between the measured Seebeck coefficient and estimated Lorenz number.

Figure 8 shows the relationship between the estimated Lorenz number from Fig. (7) and the measured Seebeck coefficient. The estimated Lorenz number decreased from 1.18 to 0.73×10^{-8} W S^{-1} K^{-2} with increasing Seebeck coefficient. In the present study, the Lorenz number decreased with increasing Seebeck coefficient as predicted by the single parabolic band model [18].

For a single parabolic band model, the Lorenz number L is a function of the reduced Fermi energy η and scattering parameter γ only, as is the Seebeck coefficient α, as shown in Eqs. (3) and (4) [18]. By using the measured Seebeck coefficients and estimated Lorenz number L shown in Fig. 8, the scattering parameter γ and the reduced Fermi energy η were solved by Eqs. (3)–(5).

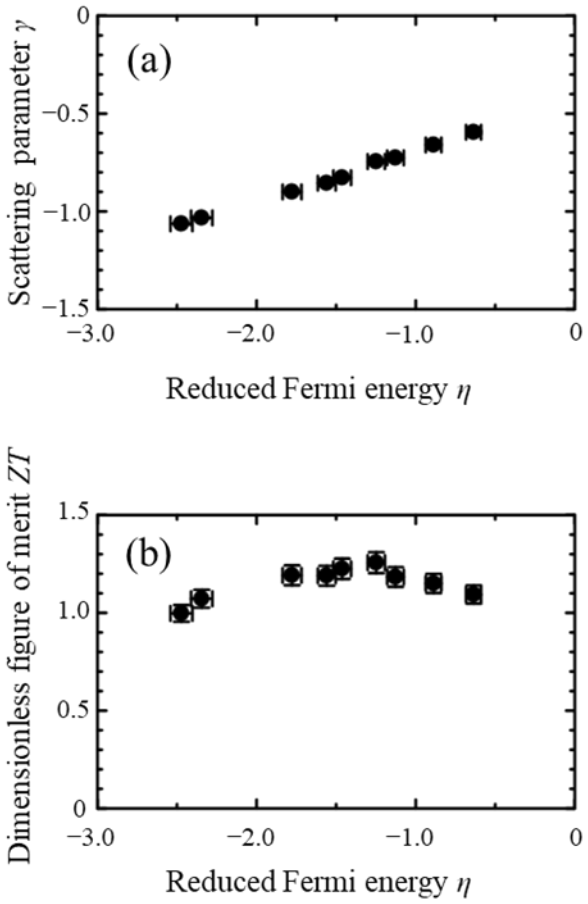

Fig. 9 The relationships between the reduced Fermi energy and the (a) scattering parameter and (b) dimensionless figure of merit (*ZT*).

Figure 9 (a) shows the relationship between the scattering parameter γ and reduced Fermi energy η. The scattering parameters for our samples ranged from −1.06 to −0.60, which indicates that the scattering mechanism of the $Bi_{0.3}Sb_{1.7}Te_{3.0}$ alloys produced by MA-HP was the mutual effect of acoustic and optical phonon scattering [22,63]. The

scattering parameter of the Bi_2Te_3 fabricated by the established melt growth method has been reported to be −0.8 to 0.1 [64]. The estimated scattering parameter was slightly smaller than that of the Bi_2Te_3 fabricated by the established melt growth method. The result indicates that the MA-HP process decreased the scattering parameters by grain refining effect [22]. The scattering parameter of $Bi_{0.5}Sb_{1.5}Te_3$ fabricated by using metal vessels measured by the temperature dependence of carrier concentration varied from −2.2 to −0.9 [22]. It was assumed that the difference in γ was due to the difference in measurement accuracy or the influence of impurities from the milling vessels [45]. According to Figure 9 (b), the ZT increased with increasing reduced Fermi energy η, peaked at 1.26 when η = −1.25, and then decreased with increasing reduced Fermi energy, qualitatively corresponding to the theoretical calculation [44]. However, the optimal value of the reduced Fermi energy is approximately −0.5 in the theoretical calculation [44]. The difference in the optimal value of the reduced Fermi energy was due to the differences in γ and κ_{phonon}. The γ was assumed as −0.22 and κ_{phonon} as 1.3 W m^{-1} K^{-1} in the theoretical calculation, which were the values of the melt grown sample. The results indicate that the optimum reduced Fermi energy for the sample fabricated by MA-HP is on the smaller side than that of the melt growth method due to the reduced γ and κ_{phonon} by MA-HP process.

These results show that the scattering mechanism at room temperature and the relationship between the *ZT* and reduced Fermi energy could be determined without the temperature dependence of the thermoelectric properties. Furthermore, it was clarified that the MA-HP process reduces the scattering parameter compared to the melt growth method. These analyses will be applicable in Bi_2Te_3-Sb_2Te_3 thermoelectric materials and have the potential to be applied in other thermoelectric materials. From these results, the slight amount of multiple doping in thermoelectric materials is a simple and effective way to evaluate the Lorenz number and scattering mechanism.

4. Conclusion

In the present study, the effects of adding lead as one of the multiple dopants in $Bi_{0.3-x}Sb_{1.7}Te_{3.01}Pb_x$ (x = 0, 0.001, 0.002, 0.003) prepared by MA-HP were investigated. From the results, the Lorenz number L and scattering parameter γ were estimated under constant temperature. The findings are summarized as follows.

(1) All of the sintered samples with x = 0–0.003 were p-type semiconductors. All of the samples consisted of dense, homogeneous, and fine grains of approximately 1 μm.

(2) The lead, added as one of the multiple dopants, acted as a hole carrier dopant, which brought a wider variation range of electrical properties than tellurium doping alone. On the other hand, the function of lead added as one of the multiple dopants was the same as that added as a single dopant, and the specific effect of multiple doping was not confirmed. The dimensionless figure of merit ZT at room temperature was affected due to the overbalance of the carrier concentration. For $0.001 \leq x \leq 0.003$, the ZT varied from 1.18 to 1.09.

(3) The Lorenz number L at room temperature was estimated to be $0.73–1.18 \times 10^{-8}$ W S^{-1} K^{-2} by assuming the phonon thermal conductivity constant and the relationship between the thermal conductivity and the electrical conductivity.

(4) The scattering parameter γ at room temperature was estimated by using the above

Lorenz number and measured Seebeck coefficients. The parameter γ varied from −1.06 to −0.60, which indicated that the scattering mechanism of the $Bi_{0.3}Sb_{1.7}Te_{3.0}$ alloys produced by MA-HP was a mutual effect of acoustic and optical phonon scattering.

(5) The relationship between the dimensionless figure of merit *ZT* and reduced Fermi energy η was obtained. The trend of the relationship corresponded to the theoretical calculation, and *ZT* showed a peak of 1.26 at $\eta = -1.25$.

Acknowledgments

The authors express gratitude to Emeritus Prof. Yasutoshi Noda (Shimane University, Japan) for valuable discussions on one-electron approximation.

References

[1] F.J. Disalvo, Thermoelectric cooling and power generation, Science 285 (1999) 703–706. https://doi.org/10.1126/science.285.5428.703.

[2] Q.H. Zhang, X.Y. Huang, S.Q. Bai, X. Shi, C. Uher, L.D. Chen, Thermoelectric devices for power generation: recent progress and future challenges, Adv. Eng. Mater. 18 (2016) 194–213. https://doi.org/10.1002/adem.201500333.

[3] J. Karni, Solar energy: the thermoelectric alternative, Nat. Mater. 10 (2011) 481–482. https://doi.org/10.1038/nmat3057.

[4] J.H. Kim, H. Cho, S.Y. Back, J.H. Yun, H.S. Lee, J.S. Rhyee, Lattice distortion and anisotropic thermoelectric properties in hot-deformed CuI-doped $Bi_2Te_{2\cdot7}Se_{0.3}$, J. Alloys Compd. 815 (2020) 152649. https://doi.org/10.1016/j.jallcom.2019.152649.

[5] S.Y. Back, H. Cho, S. Byeon, H. Jin, J.S. Rhyee, Effective phonon scattering and enhancement of thermoelectric performance in Ga-excess $Bi_{0.4}Sb_{1.6}Te_3$ compounds, Curr. Appl. Phys. 20 (2020) 1036–1040. https://doi.org/10.1016/j.cap.2020.06.024.

[6] Y. Zhang, C. Xing, Y. Liu, M. Li, K. Xiao, P. Guardia, S. Lee, X. Han, A. Ostovari Moghaddam, J. Josep Roa, J. Arbiol, M. Ibáñez, K. Pan, M. Prato, Y.

Xie, A. Cabot, Influence of copper telluride nanodomains on the transport properties of *n*-type bismuth telluride, Chem. Eng. J. 418 (2021) 129374. https://doi.org/10.1016/j.cej.2021.129374.

[7] M. Bumrungpon, I. Morioka, R. Yasufuku, T. Hirai, K. Hanasaku, K. Hirota, K. Takagi, K. Hasezaki, The critical point of average grain size in phonon thermal conductivity of fine-grained undoped lead telluride, Mater. Trans. 61 (2020) 2025–2029. https://doi.org/10.2320/matertrans.MT-M2020069.

[8] L.D. Ivanova, Y. V. Granatkina, A.G. Mal'chev, I.Y. Nikhezina, S.P. Krivoruchko, M.I. Zaldastanishvili, T.S. Vekua, N.M. Sudak, Preparation and thermoelectric properties of microcrystalline lead telluride, Inorg. Mater. 56 (2020) 791–798. https://doi.org/10.1134/S0020168520080063.

[9] B.B. Zhu, C. Chen, Z.C. Yao, J.Y. Chen, C. Jia, Z.H. Wang, R.M. Tian, L. Tao, F. Xue, H.H. Hng, Multiple doped ZnO with enhanced thermoelectric properties, J. Eur. Ceram. Soc. 41 (2021) 4182–4188. https://doi.org/10.1016/j.jeurceramsoc.2021.01.054.

[10] Z. Shi, F. Gao, J. Xu, J. Zhu, Y. Zhang, T. Gao, M. Qin, M. Reece, H. Yan, Two–step processing of thermoelectric $(Ca_{0.9}Ag_{0.1})_3Co_4O_9$ /nano–sized Ag composites with high *ZT*, J. Eur. Ceram. Soc. 39 (2019) 3088–3093.

https://doi.org/10.1016/j.jeurceramsoc.2019.04.004.

[11] D. Rabina, A. Meshulam, D. Fuks, Y. Gelbstein, High entropy alloy on single sub-lattice in MNiSn compound: stability and thermoelectric properties, J. Alloys Compd. 874 (2021) 159940. https://doi.org/10.1016/j.jallcom.2021.159940.

[12] I. Ioannou, P.S. Ioannou, A. Delimitis, Y. Gelbstein, I.J. Giapintzakis, T. Kyratsi, High thermoelectric performance of *p*-type half-Heusler (Hf,Ti)Co(Sb,Sn) solid solutions fabricated by mechanical alloying, J. Alloys Compd. 858 (2021) 158330. https://doi.org/10.1016/j.jallcom.2020.158330.

[13] J. Shuai, H. Geng, Y. Lan, Z. Zhu, C. Wang, Z. Liu, J. Bao, C.-W. Chu, J. Sui, Z. Ren, Higher thermoelectric performance of Zintl phases $(Eu_{0.5}Yb_{0.5})_{1-x}Ca_xMg_2Bi_2$ by band engineering and strain fluctuation, Proc. Natl. Acad. Sci. 113 (2016) E4125–E4132. https://doi.org/10.1073/PNAS.1608794113.

[14] A. Zevalkink, J. Swallow, G.J. Snyder, Thermoelectric properties of Zn-doped $Ca_5In_2Sb_6$, Dalt. Trans. 42 (2013) 9713–9719. https://doi.org/10.1039/c3dt50428j.

[15] W. Liu, J. Hu, S. Zhang, M. Deng, C.G. Han, Y. Liu, New trends, strategies and opportunities in thermoelectric materials: a perspective, Mater. Today Phys. 1 (2017) 50–60. https://doi.org/10.1016/j.mtphys.2017.06.001.

[16] M. Stordeur, Valence band structure and the thermoelectric figure-of-merit of

$(Bi_{1-x}Sb_x)_2Te_3$ crystals, in: D.M. Rowe (Ed.), CRC Handbook of Thermoelectrics, CRC Press, Taylor & Francis Group, Boca Raton, Florida, 1995, pp. 239–255.

[17] M. Orihashi, Y. Noda, L. Chen, T. Hirai, Carrier concentration dependence of thermal conductivity of iodine-doped *n*-type PbTe, Mater. Trans. JIM. 41 (2000) 1282–1286. https://doi.org/10.2320/matertrans1989.41.1282.

[18] H.S. Kim, Z.M. Gibbs, Y. Tang, H. Wang, G.J. Snyder, Characterization of Lorenz number with Seebeck coefficient measurement, APL Mater. 3 (2015) 041506. https://doi.org/10.1063/1.4908244.

[19] R.S. Allgaier, W.W. Scanlon, Mobility of electrons and holes in PbS, PbSe, and PbTe between room temperature and 4.2°K, Phys. Rev. 111 (1958) 1029–1037. https://doi.org/10.1103/PhysRev.111.1029.

[20] D.M. Brown, R. Bray, Analysis of lattice and ionized impurity scattering in *p*-type germanium, Phys. Rev. 127 (1962) 1593–1602. https://doi.org/10.1103/PhysRev.127.1593.

[21] G.S. Noals, J. Sharp, H.J. Goldsmid, Thermoelectrics Basic Principles and New Materials Developments, Springer, Berlin, Heidelberg, 2001, pp.111–121.

[22] K. Hasezaki, T. Hamachiyo, M. Ashida, T. Ueda, Y. Noda, Thermoelectric properties and scattering factors of finely grained Bi_2Te_3-related materials

prepared by mechanical alloying, J. Japan Inst. Metals, 74 (2010) 623–628. https://doi.org/10.2320/jinstmet.74.623.

[23] H. Mamur, M.R.A. Bhuiyan, F. Korkmaz, M. Nil, A review on bismuth telluride (Bi_2Te_3) nanostructure for thermoelectric applications, Renew. Sustain. Energy Rev. 82 (2018) 4159–4169. https://doi.org/10.1016/j.rser.2017.10.112.

[24] H. Scherrer, S. Scherrer, Thermoelectric properties of bismuth antimony telluride solid solutions, in: D.M. Rowe (Ed.), Thermoelectrics Handbook Macro to Nano, CRC Press, Taylor & Francis Group, Boca Raton, Florida, 2006, ch. 27.

[25] K. Hasezaki, M. Nishimura, M. Umata, H. Tsukuda, M. Araoka, Mechanical alloying of BiTe and BiSbTe thermoelectric materials, Mater. Trans. JIM. 35 (1994) 428–432. https://doi.org/10.2320/matertrans1989.35.428.

[26] Y. Ma, Q. Hao, B. Poudel, Y. Lan, B. Yu, D. Wang, G. Chen, Z. Ren, Enhanced thermoelectric figure-of-merit in *p*-type nanostructured bismuth antimony tellurium alloys made from elemental chunks, Nano Lett. 8 (2008) 2580–2584. https://doi.org/10.1021/nl8009928.

[27] M. Zakeri, M. Allahkarami, G. Kavei, A. Khanmohammadian, M.R. Rahimipour, Synthesis of nanocrystalline Bi_2Te_3 via mechanical alloying, J. Mater. Process. Technol. 209 (2009) 96–101. https://doi.org/10.1016/j.jmatprotec.2008.01.027.

[28] J. Asai, M. Bumrungpon, T. Tsubochi, T. Kanaya, M. Tachii, T. Maeda, K. Hasezaki, Shift of tellurium solid-solubility limit and enhanced thermoelectric performance of bismuth antimony telluride milled with yttria-stabilized zirconia balls and vessels, J. Eur. Ceram. Soc. 41 (2021) 188–194. https://doi.org/10.1016/j.jeurceramsoc.2021.09.019.

[29] H.L. Zhuang, Y. Pan, F.H. Sun, J. Dong, J. Pei, Asfandiyar, B. Cai, H. Hu, H. Tang, J.F. Li, Thermoelectric Cu-doped $(Bi,Sb)_2Te_3$: performance enhancement and stability against high electric current pulse, Nano Energy. 60 (2019) 857–865. https://doi.org/10.1016/j.nanoen.2019.04.021.

[30] K. Kim, G. Kim, H. Lee, K.H. Lee, W. Lee, Band engineering and tuning thermoelectric transport properties of *p*-type $Bi_{0.52}Sb_{1.48}Te_3$ by Pb doping for low-temperature power generation, Scr. Mater. 145 (2018) 41–44. https://doi.org/10.1016/j.scriptamat.2017.10.009.

[31] Z. Wei, C. Wang, J. Zhang, J. Yang, Z. Li, Q. Zhang, P. Luo, W. Zhang, E. Liu, J. Luo, Precise regulation of carrier concentration in thermoelectric BiSbTe alloys via magnetic doping, ACS Appl. Mater. Interfaces 12 (2020) 20653–20663. https://doi.org/10.1021/acsami.0c02408.

[32] C.K. Lin, M.S. Chen, R.T. Huang, Y.C. Cheng, P.Y. Lee, Thermoelectric

properties of alumina-doped $Bi_{0.4}Sb_{1.6}Te_3$ nanocomposites prepared through mechanical alloying and vacuum hot pressing, Energies 8 (2015) 12573–12583. https://doi.org/10.3390/en81112323.

[33] F. Wu, H. Song, J. Jia, X. Hu, Effects of Ce, Y, and Sm doping on the thermoelectric properties of Bi_2Te_3 alloy, Prog. Nat. Sci. Mater. Int. 23 (2013) 408–412. https://doi.org/10.1016/j.pnsc.2013.06.007.

[34] Y. Wu, R. Zhai, T. Zhu, X. Zhao, Enhancing room temperature thermoelectric performance of *n*-type polycrystalline bismuth-telluride-based alloys via Ag doping and hot deformation, Mater. Today Phys. 2 (2017) 62–68. https://doi.org/10.1016/j.mtphys.2017.09.001.

[35] H.R. Williams, R.M. Ambrosi, K. Chen, U. Friedman, H. Ning, M.J. Reece, M.C. Robbins, K. Simpson, K. Stephenson, Spark plasma sintered bismuth telluride-based thermoelectric materials incorporating dispersed boron carbide, J. Alloys Compd. 626 (2015) 368–374. https://doi.org/10.1016/j.jallcom.2014.12.010.

[36] M.Y. Kim, Y.H. Yeo, D.H. Park, T.S. Oh, Thermoelectric characteristics of the $(Bi,Sb)_2(Te,Se)_3$ nanocomposites processed with nanoparticle dispersion, Ceram. Int. 38S (2012) S529–S533. https://doi.org/10.1016/j.ceramint.2011.05.069.

[37] K. Ahmad, C. Wan, P. an Zong, Thermoelectric properties of BiSbTe/graphene

nanocomposites, J. Mater. Sci. Mater. Electron. 30 (2019) 11923–11930. https://doi.org/10.1007/s10854-019-01538-z.

[38] J.F. Li, J. Liu, Effect of nano-SiC dispersion on thermoelectric properties of Bi_2Te_3 polycrystals, Phys. Stat. Sol. (a), 203 (2006) 3768–3773. https://doi.org/10.1002/pssa.200622011.

[39] Y. Pan, Y. Qiu, I. Witting, L. Zhang, C. Fu, J.W. Li, Y. Huang, F.H. Sun, J. He, G.J. Snyder, C. Felser, J.F. Li, Synergistic modulation of mobility and thermal conductivity in $(Bi,Sb)_2Te_3$ towards high thermoelectric performance, Energy Environ. Sci. 12 (2019) 624–630. https://doi.org/10.1039/c8ee03225d.

[40] I.T. Witting, J.A. Grovogui, V.P. Dravid, G.J. Snyder, Thermoelectric transport enhancement of Te-rich bismuth antimony telluride ($Bi_{0.5}Sb_{1.5}Te_{3+x}$) through controlled porosity, J. Mater. 6 (2020) 532–544. https://doi.org/10.1016/j.jmat.2020.04.001.

[41] K.T. Kim, T.S. Lim, G.H. Ha, Improvement in thermoelectric properties of *n*-type bismuth telluride nanopowders by hydrogen reduction treatment, Rev. Adv. Mater. Sci. 28 (2011) 196–199.

[42] J. Jang, B.K. Min, B.S. Kim, S.J. Joo, H.S. Lee, J.E. Lee, Development of *p*-type $Bi_{2-x}Sb_xTe_3$ thermoelectric materials for power generation application exploiting

synergetic effect of Sb alloying and repress process, Appl. Surf. Sci. 508 (2020) 145236. https://doi.org/10.1016/j.apsusc.2019.145236.

[43] M. Kitamura, K. Hasezaki, Effect of mechanical alloying on thermal conductivity of Bi_2Te_3-Sb_2Te_3, Mater. Trans. 57 (2016) 2153–2157. https://doi.org/10.2320/matertrans.M2016169.

[44] K. Uemura, I. Nishida, Thermoelectric Semiconductor and Its Applications, Nikkankougyou Shinbunsha, Tokyo, 1988, pp.148–150 and 167–169.

[45] M. Bumrungpon, K. Hirota, K. Takagi, K. Hanasaku, T. Hirai, I. Morioka, R. Yasufuku, M. Kitamura, K. Hasezaki, Synthesis and thermoelectric properties of bismuth antimony telluride thermoelectric materials fabricated at various ball-milling speeds with yttria-stabilized zirconia ceramic vessel and balls, Ceram. Int. 46 (2020) 13869–13876. https://doi.org/10.1016/j.ceramint.2020.02.180.

[46] L.P. Hu, T.J. Zhu, Y.G. Wang, H.H. Xie, Z.J. Xu, X.B. Zhao, Shifting up the optimum figure of merit of *p*-type bismuth telluride-based thermoelectric materials for power generation by suppressing intrinsic conduction, NPG Asia Mater. 6 (2014) e88. https://doi.org/10.1038/am.2013.86.

[47] Z. Tang, L. Hu, T. Zhu, X. Liu, X. Zhao, High performance *n*-type bismuth telluride based alloys for mid-temperature power generation, J. Mater. Chem. C.

3 (2015) 10597–10603. https://doi.org/10.1039/C5TC02263K.

[48] K. Hasezaki, S. Wakazuki, T. Fujii, M. Kitamura, Constituent element addition to *n*-type $Bi_2Te_{2.67}Se_{0.33}$ thermoelectric semiconductor without harmful dopants by mechanical alloying, Mater. Trans. 57 (2016) 1001–1005. https://doi.org/10.2320/matertrans.M2016031.

[49] J. Li, Q. Tan, J.F. Li, D.W. Liu, F. Li, Z.Y. Li, M. Zou, K. Wang, BiSbTe-based nanocomposites with high *ZT*: the effect of SiC nanodispersion on thermoelectric properties, Adv. Funct. Mater. 23 (2013) 4317–4323. https://doi.org/10.1002/adfm.201300146.

[50] B. Madavali, H. Kim, S.J. Hong, Reduction of thermal conductivity in Al_2O_3 dispersed *p*-type bismuth antimony telluride composites, Mater. Chem. Phys. 233 (2019) 9–15. https://doi.org/10.1016/j.matchemphys.2019.05.023.

[51] K.C. Lukas, W.S. Liu, G. Joshi, M. Zebarjadi, M.S. Dresselhaus, Z.F. Ren, G. Chen, C.P. Opeil, Experimental determination of the Lorenz number in $Cu_{0.01}Bi_2Te_{2.7}Se_{0.3}$ and $Bi_{0.88}Sb_{0.12}$, Phys. Rev. B - Condens. Matter Mater. Phys. 85 (2012) 205410. https://doi.org/10.1103/PhysRevB.85.205410.

[52] C.H. Su, Experimental determination of lattice thermal conductivity and Lorenz number as functions of temperature for *n*-type PbTe, Mater. Today Phys. 5

(2018) 58–63. https://doi.org/10.1016/j.mtphys.2018.05.005.

[53] S. Turenne, T. Clin, D. Vasilevskiy, R.A. Masut, Finite element thermomechanical modeling of large area thermoelectric generators based on bismuth telluride alloys, J. Electron. Mater. 39 (2010) 1926–1933. https://doi.org/10.1007/s11664-009-1049-z.

[54] M. Orihashi, Y. Noda, K. Hasezaki, Surface texture of Bi_2Te_3-based materials deformed under pressure-current heating, Int. Conf. Thermoelectr. ICT, Proc. (2007) 86–89. https://doi.org/10.1109/ICT.2007.4569430.

[55] K. Yamauchi, M. Takashiri, Highly oriented crystal growth of nanocrystalline bismuth telluride thin films with anisotropic thermoelectric properties using two-step treatment, J. Alloys Compd. 698 (2017) 977–983. https://doi.org/10.1016/j.jallcom.2016.12.284.

[56] C. Chen, B. Zhang, D. Liu, Z. Ge, Thermoelectric properties of $Cu_yBi_xSb_{2-x-y}Te_3$ alloys fabricated by mechanical alloying and spark plasma sintering, Intermetallics 25 (2012) 131–135. https://doi.org/10.1016/j.intermet.2012.02.018.

[57] M. Fusa, N. Yamamoto, K. Hasezaki, Measurement of seebeck coefficient and conductive behaviors of $Bi_2Te_{3-x}Se_x$ (x = 0.15–0.6) thermoelectric

semiconductors without harmful dopants, Mater. Trans. 55 (2014) 942–946. https://doi.org/10.2320/matertrans.MB201301.

[58] N.D. Lowhorn, W. Wong-Ng, Z.Q. Lu, E. Thomas, M. Otani, M. Green, N. Dilley, J. Sharp, T.N. Tran, Development of a Seebeck coefficient standard reference material, Appl. Phys. A Mater. Sci. Process. 96 (2009) 511–514. https://doi.org/10.1007/s00339-009-5191-5.

[59] K. Hirota, K. Takagi, K. Hanasaku, K.L. Hasezaki, H. Saito, S. Hata, K. Hasezaki, Carbon observation by electron energy-loss spectroscopy and thermoelectric properties of graphite added bismuth antimony telluride prepared by mechanical alloying-hot pressing, Intermetallics 109 (2019) 1–7. https://doi.org/10.1016/j.intermet.2019.03.005.

[60] T.M. Tritt, Thermal Conductivity: Theory, Properties, and Applications, Kluwer Academic/Plenum Publishers, New York, 2004, pp. 3–9 and 187–195.

[61] L. Zhao, W. Qiu, Y. Sun, L. Chen, H. Deng, L. Yang, X. Shi, J. Tang, Enhanced thermoelectric performance of $Bi_{0.3}Sb_{1.7}Te_3$ based alloys by dispersing TiC ceramic nanoparticles, J. Alloys Compd. 863 (2021) 158376. https://doi.org/10.1016/j.jallcom.2020.158376.

[62] K. Hirota, M. Kitamura, K. Takagi, K. Hasezaki, Thermoelectric behaviors of

$Bi_{0.3}Sb_{1.7}Te_{3.0}$ with excess or deficiency of tellurium prepared by mechanical alloying followed by hot pressing, Mater. Trans. 59 (2018) 1233–1238. https://doi.org/10.2320/matertrans.MF201704.

[63] D.L. Young, T.J. Coutts, V.I. Kaydanov, A.S. Gilmore, W.P. Mulligan, Direct measurement of density-of-states effective mass and scattering parameter in transparent conducting oxides using second-order transport phenomena, J. Vac. Sci. Technol. A 18 (2000) 2978–2985. https://doi.org/10.1116/1.1290372.

[64] C.B. Satterthwaite, R.W. Ure, Electrical and thermal properties of Bi_2Te_3, Phys. Rev. 108 (1957) 1164–1170. https://doi.org/10.1103/PhysRev.108.1164.

Figure captions

Fig. 1 XRD patterns (2θ = 10–110°) of $Bi_{0.3-x}Sb_{1.7}Te_{3.01}Pb_x$ (x = 0, 0.003) sintered disks prepared by MA-HP and $Bi_{0.3}Sb_{1.7}Te_{3.0}$ main indices [56]. The standard peaks correspond to $Bi_{0.3}Sb_{1.7}Te_{3.0}$ (ICSD #184248).

Fig. 2 DTA curves for pestle-ground, sintered disks of $Bi_{0.3-x}Sb_{1.7}Te_{3.01}Pb_x$ (x = 0 and 0.003) prepared by MA-HP.

Fig. 3 SEM micrographs of the cross-section of sintered disks with (a) x = 0 and (b) x = 0.003. SEM micrographs of the fracture surface of sintered disks with (c) x = 0 and (d) x = 0.003.

Fig. 4 (a) A STEM micrograph of the cross-section of the sintered disk with x = 0.003 and the elemental distributions of (b) Sb, (c) Te, (d) Bi, and (e) Pb determined by EDS.

Fig. 5 The relationships between the room-temperature thermoelectric properties and the amount of additive lead (x) for $Bi_{0.3-x}Sb_{1.7}Te_{3.01}Pb_x$. (a) Seebeck coefficient, (b) electrical conductivity, (c) thermal conductivity, and (d) dimensionless figure of merit (ZT).

Fig. 6 The relationships between the room-temperature thermoelectric properties and the amount of additive tellurium (y) for $Bi_{0.3}Sb_{1.7}Te_{3.0+y}$. (a) Seebeck coefficient, (b) electrical conductivity, (c) thermal conductivity, and (d) dimensionless figure of merit

(*ZT*).

Fig. 7 The relationship between thermal and electrical conductivity. The quadratic curve shows $\kappa = (1.50 \times 10^{-11}\sigma + 1.62 \times 10^{-6})\sigma + 0.902$.

Fig. 8 The relationship between the measured Seebeck coefficient and estimated Lorenz number.

Fig. 9 The relationships between the reduced Fermi energy and the (a) scattering parameter and (b) dimensionless figure of merit (*ZT*).

Table 1 Absolute and relative densities of $Bi_{0.3-x}Sb_{1.7}Te_{3.01}Pb_x$ and $Bi_{0.3}Sb_{1.7}Te_{3.0+y}$.